Augmented Prediction of Turbulent Flows via Sequential Estimators Sensitivity of State Estimation to Density of Time Sampling for Available Observation

Marcello Meldi

Augmented Prediction of Turbulent Flows via Sequential Estimators

Sensitivity of State Estimation to Density of Time Sampling for Available Observation

Marcello Meldi[1,2]

Abstract

A sensitivity analysis of new methodological approaches for state estimation (Meldi and Poux J. Comput. Phys. **347**, 207–234, 2017) is proposed in this manuscript. The performance of the estimator is tested via the analysis of a number of aspects that play a major role in the augmented prediction process, such as the density in time sampling of available observation, the placement of sensors and the interaction with boundary conditions. The work is developed for the turbulent spatially evolving mixing layer test case, using high precision DNS samples as observation and Smagorinsky LES as underlying model. A number of estimators combining LES with DNS data integrated via sensors are performed, varying the frequency of time sampling of observation $f_T = 1/\Delta_T$, where Δ_T is the period between successive assimilation phases. It is concluded that if $\Delta_T \leq\approx 0.5 t_A$, where t_A is the characteristic average advection time, the prediction via estimator shows minimal differences i.e. the process of state estimation has reached convergence. This relation can be interpreted as a threshold for converged state estimation. However, the results show as well that a linear converge towards pure model performance is not obtained for every physical quantity with progressive decrease of f_T, while eventually pure model results are obtained for $f_T \rightarrow 0$. In addition, the effect of upstream boundary conditions over the state estimation are investigated and strategies for optimized positions of sensors are derived.

Keywords State estimation · Data assimilation · Kalman filter · Large Eddy Simulation

✉ Marcello Meldi
marcello.meldi@ensma.fr

[1] Poitiers - Institut Pprime, Department of Fluid Flow, Heat Transfer and Combustion, CNRS - ENSMA - Université de Poitiers, UPR 3346, SP2MI - Teleport, 211 Bd. Marie et Pierre Curie, B.P. 30179, F86962 Futuroscope Chasseneuil Cedex, France

[2] Aix-Marseille Univ., CNRS, Centrale Marseille, M2P2 Marseille, France

1 Introduction

Among the numerous research aspects which can be investigated in the analysis of complex flow configurations of industrial interest, the accurate prediction of turbulent flows is one of the ultimate open challenges. Analyses performed via classical tools, such as experiments and numerical simulation are strongly affected by fundamental drawbacks which can not be completely excluded and limit the level of confidence in the results obtained. This aspect is fundamental for transport engineering applications and environmental studies, where advances in the performance of the order of 1% represent a huge improvement in optimization of usage of resources [1]. Experimental Fluid Mechanics (EFD) provides a local description of flow dynamics via measurements which are sampled by sensors. While numerous, sophisticated techniques have been developed in the last decades, a complete reconstruction of the flow behavior in the whole physical domain from local measurements is problematic because of the non-linear, strongly inertial behavior of turbulence. While reduced-order models, such as POD [2], have been extensively used for this purpose, they usually provide an incomplete reconstruction of turbulent flows for the aforementioned reasons.

On the other hand, Computational Fluid Dynamics (CFD) can provide flow characteristics on large physical domains, owing to the numerical resolution of set of differential equations. However, the resolution of these numerical systems is affected as well by errors / epistemic uncertainties. In this case, the boundary conditions / turbulence modeling [3, 4] cannot exactly reproduce the fine perturbations and inhomogeneity of the real flow, which are unknown a priori but they are ultimately responsible for the emergence of turbulent regimes. The main technological limit that needs to be faced is that traditional tools used for the investigation of turbulent flows are affected by a bias, which stems from uncertainties of a completely different nature when considering experiments / numerical simulation. Because of this reason, major difficulties arise to obtain robust information even when performing direct comparison of experiments and numerical results.

New methodological approaches coming from Estimation Theory (ET) [5] and Data Assimilation (DA) [6] are nowadays used to obtain an optimal state estimation of turbulent flows via integration of different sources of information. One of the key aspects of these research strategies is accounting for the level of uncertainty / stochasticity intimately associated with these sources of information. These techniques, which are usually referred to as *estimators*, are used to perform a strong coupling between experimental / numerical data and they have the potential to exclude the bias which can not be identified in the two methods alone. The interest of the scientific community on these methods is confirmed by an increasingly number of studies in the literature in recent years [7–9]. Along with successful advances achieved in this field, new horizons of investigation for robust applications of these techniques must be explored to obtain general guidelines of usage.

It the present work, the convergence and application properties of state estimation obtained via a recent sequential tool proposed by Meldi and Poux [10] is investigated. This method integrates available observation, local in space and time, in a classical CFD solver. The sensitivity of the state estimation to a number of different aspects is investigated: density of the time sampling of observation, positioning of the sensors where observation is provided and interaction of the state estimation process with boundary conditions. The study is carried out via analysis of the turbulent spatially evolving mixing layer flow configuration.

The paper is organized as follows. In Section 2, the test case of investigation is presented. In Section 3 the relevance of the objectives of the present analysis towards improved

sequential state estimation are discussed. In Section 4, the sensitivity analysis for the instantaneous flow fields and their statistical properties is developed. In Section 5, the set-up of the test case for the LES is modified, in order provide a more realistic example of sequential state estimation using different sources of information. Finally, in Section 6 the conclusive remarks are drawn. Appendix A is dedicated to a comprehensive description of the sequential estimator, in order to focus the discussion in the manuscript towards the scientific objectives.

2 Test Case of Investigation: Turbulent Spatially Evolving Mixing Layer

The turbulent spatially evolving mixing layer [11–15] is a classical test case of investigation in fluid mechanics studies. In fact, shear effects which govern the flow evolution in numerous industrial and environmental applications are here isolated and can be unambiguously studied. In the *spatially evolving* test case, the shear effect is produced by the interaction of two homogeneous co-flows, which are characterized by different asymptotic velocities U_1 and U_2. This interaction results in the emergence of a wake, which can evolve to fully turbulent behavior if the Reynolds number is large enough. In this analysis, a value of $Re_\delta = \delta(U_1 - U_2)/2\nu = 100$ is chosen. δ is the the value of the vorticity thickness imposed at the inlet and it is a measure of the transition between the two asymptotic regimes characterized by the velocities U_1 and U_2, respectively. The streamwise direction x indicates the asymptotic trajectory of the flow. The velocity gradient is observed in the normal direction y. Finally, z is the spanwise direction. The characteristic parameter $\alpha = (U_1 - U_2)/(U_1 + U_2)$ which measures the loss of symmetry of the configuration and represents the ratio of shear effects vs mean advection is set to $\alpha = 0.27$. The flow is investigated in a physical domain of size $[x \times y \times z] \in [0, 24 \times -9, 6 \times -3, 3]$. The physical domain is normalized over the characteristic primary instability length $\Lambda = 15.4\delta$. Such a large domain, in particular in the normal direction y, has been chosen in order to reduce the effect of boundary conditions over the flow evolution. More precisely, the boundary condition imposed are:

- a velocity hyperbolic tangent profile $U = 0.5(U_1 + U_2) + 0.5(U_1 - U_2)\tanh(2y/\delta)$ for the inlet. This base velocity profile is complexified with the addition of spanwise spatial modes and white noise time perturbation to accelerate the transition towards a turbulent regime [10]. These perturbations, which exhibit a maximum magnitude of $\approx 2\%$ of the laminar streamwise velocity for $y = 0$ and are applied to every component of the velocity field, decrease following a Gaussian law with increasing distance from the center-line.
- an advective velocity condition at the outlet, in order to reduce as much as possible reflective waves in the physical domain
- a traction-free condition on both normal planes $(x - z)$
- a periodic boundary condition on both spanwise planes $(x - y)$

Using this set-up, the flow exhibits a progressive transition to turbulence for $x \approx 10\Lambda$ after an initial laminar evolution which is governed by the inlet boundary condition. A visual representation of the test case investigated and the instantaneous behavior of the inlet for $t = 0$ are shown for DNS data in Fig. 1.

A database of simulations has been generated to perform the sensitivity analysis. For every simulation, the numerical discretization of the Navier-Stokes equations is based on centered second order schemes for the spatial derivatives. A second order backward scheme

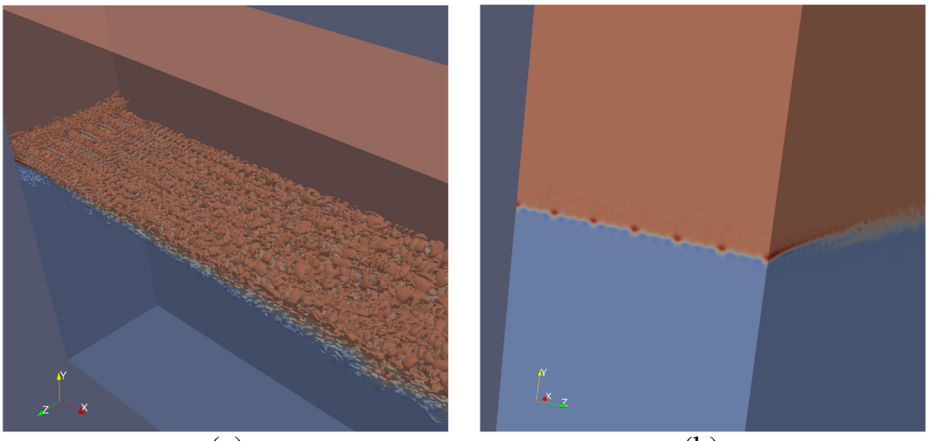

Fig. 1 Representation of the spatially evolving mixing layer via DNS data. **a** Isocontours of the instantaneous Q criterion (colored with the velocity field) are represented along with the physical domain of investigation. The red color is associated with the asymptotic flow at higher velocity U_1, the blue color with the asymptotic flow at lower velocity U_2. **b** Zoom of an instantaneous velocity magnitude profile around the center-line for $x = 0$, where the included spatial modes and the white noise time perturbation at the inlet are clearly observable

has been used for the discretization of the time derivative. The database consists of a single Direct Numerical Simulation (DNS) and 13 Large Eddy Simulations (LES). The size of the mesh resolution has been chosen with respect to an estimation of the Kolmogorov scale η based on the bulk flow quantities. The resolution of the DNS has been chosen following classical recommendations. In particular, the mesh distribution is uniform in the x and z directions. For the normal direction y, a uniform spacing has been imposed in the central range $[-\Lambda,\ \Lambda]$, while the elements are coarsened following a geometric progression as they approach the boundaries in the normal direction. The structure of the mesh for the LES is qualitatively the same, but mesh elements are 4 times larger in the x and y directions and 2 times larger in the y direction (range $[-\Lambda,\ \Lambda]$). A summary of the mesh features is reported in Table 1. Finally, a constant time step has been chosen as $\Delta t = 0.01 t_A = 0.01 \times 2\Lambda/(U_1 + U_2)$. t_A is the average advection characteristic time in the wake. This choice implies that the condition $CFL < 0.35$ is respected at every time step for the DNS, and even $CFL < 0.09$ for the less refined LES simulations. For LES, the turbulence closure is performed via the classical Smagorinsky model [16].

Numerical simulations are started from a developed DNS solution, which is interpolated on the grid used for LES. The total simulation time is equal to 200 characteristic times t_A (equivalent to 20000 time steps) and averages are performed for $t \geq 50 t_A$. This delay has

Table 1 Numerical details of the meshes used for the simulations. The value of Δy provided represents the resolution in the range $y \in [-1, 1]$ in Λ units. η is the bulk flow Kolmogorov scale

Simulation	Δx	Δy	Δz	n_x	n_y	n_z	Nr. elem.
DNS	5.86η	2.93η	3.5η	384	163	160	10^7
LES	23.44η	5.86η	14η	96	89	40	$3.4 \cdot 10^5$

been chosen i) to allow the LES simulation to properly evolve on the coarse grid and ii) to provide a suitable synchronization time for the DA estimator.

Changes to the general set-up have been performed for some LES simulation of the database, in order to analyze specific aspects of state estimation. These changes will be described when needed in the following sections.

3 Numerical Strategy & Objectives of Investigation

The numerical elements used for the analysis are now described. It is reminded that the Kalman estimators obtain a state estimation of a random process accounting for two sources of information: a *model*, which provides a continuous approximated prediction of the quantity of investigation and some *observation*, which is usually local in space and time and provided for a number of sensors in the physical domain. In this work, the resulting Kalman estimator is defined by the integration of:

- *Model*: Smagorinsky LES
- *Observation*: data sampled from the DNS in the form of instantaneous velocities U_x, U_y and U_z. The observation is not provided in the whole physical domain, but it is limited to a cloud of sensors which are sampled in two different regions of the physical domain which will be described at the end of the present section. In order to allow comparisons with previous analyses on the same test case [10], a total number of 1000 sensors has been chosen.

The uncertainty in the DNS data and the LES results has been evaluated using Eq. 13. In DNS $\nu_{SGS} = 0$ and the mesh elements are more refined (lower Δl values), which implies that Eq. 13 provides a lower uncertainty when compared with LES. Thus, Eq. 13 correctly sets the stage for consistent DA application, because DNS results are assumed to be much more precise than LES prediction and thus the confidence in the observation is much higher than the confidence in the model.

This test case has been chosen because of a number of favorable characteristics. A first fundamental aspect regards its physical features. In fact, a progressive transition from a laminar unsteady state towards turbulence is observed for $x > 10\Lambda$ moving downstream from the inlet. While the DNS accurately captures this transition, the interaction between inlet boundary condition, lower mesh resolution and Smagorinsky sub-grid scale model introduces an unwanted eddy viscosity ν_{SGS} effect upstream in LES, which affects the global prediction of the statistical physical quantities [17, 18]. For this reason, the Kalman observer is employed to improve the characteristics of the LES simulation via integration of DNS data. The present analysis aims for providing advancement to four open questions about robustness properties of sequential Data Assimilation using the reduced-order Kalman filter estimator proposed by the research group [10]. Therefore, the sensitivity of the estimator to four different aspects will be investigated:

1. **Density in time of the observation provided**. The sequential model here employed uses the state estimation produced for basic improvement of the model. In fact, the solution provided by the estimator is used in the following time step of the model as source for time advancement. However, if the period ΔT between consecutive observations is large with respect to the simulation time step of the model or the characteristic evolution time of the flow, the beneficial effect of the state estimation is simply excluded in the same way an initial condition is forgotten after a transient. The sensitivity of the

estimator to density in time sampling of the observation is investigated performing 8 different simulations. For each of them, a different value of the constant frequency of DNS data acquisition $f_T = 1/\Delta_T$, $\Delta_T = n_T 10\Delta t$ is imposed. The values chosen for f_T correspond to the values of $n_T = 1, 2, 5, 10, 20, 50, 100, 200$. This means that in the first case DNS data will be integrated in the numerical model every 10 time steps, while in the latter case it will be every 2000 time steps. The DNS time signal is not filtered in the present work. It is considered to be raw data so that the performance of the estimator with respect to the signal frequency is analyzed in the worst possible scenario. Each application will be referred to as DA-LES-n_T. For each of these runs, the 1000 samples are placed in a box of size $x \times y \times z = [6, 12] \times [-1, 1] \times [-3, 3]$ in Λ units. 480 sensors have been placed using an homogeneous distribution, while the rest has been placed randomly. A representation of mesh elements including sensors is shown in Fig. 2.

2. **Interaction with boundary conditions**. The boundary conditions themselves, as rightly pointed out by a reviewer, act as a sort of Data Assimilation procedure because they enforce a prescribed behavior on the surface of the domain at each time step. This is particularly true for the inlet boundary condition, which governs the threshold of transition towards a turbulent regime. However, a closer look at the inlet boundary condition for DNS and LES highlights two fundamental differences. First, the under-resolution for LES in the normal and spanwise direction results in a very different *discretized* velocity profile which is imposed. Second, the white noise time perturbation imposed changes for every simulation, and this aspect arguably has an impact when numerical observation is integrated within the model. In conclusion, the inlet boundary condition assimilates slightly different information on every numerical simulation, and these differences are amplified when comparing DNS and LES. Thus, the interaction between field DA via Kalman estimator and boundary conditions deserves investigation. This is a second reason for which this test case has been chosen, because here these effects are

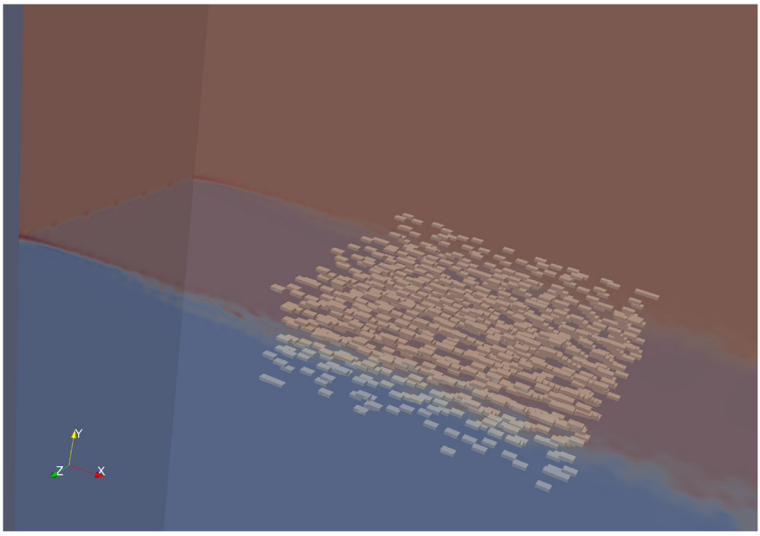

Fig. 2 Sensor placement for the application of the Kalman estimator

mostly isolated from other dynamic aspects that could not be excluded in other flow configurations.

3. **Placement of sensors**. While previous studies [10] highlighted that sequential Data Assimilation of turbulent regimes are mostly affected by a high density of observation in time when compared with space density, it is also true that sequential estimators appear to be more effective in propagating information downstream than upstream [1]. In addition, with reference to the previous item, one could argue if a high proximity between the inlet and the sensors could result in numerical instability. In order to investigate this feature, an additional Kalman estimator run has been performed for the most critical case $n_T = 1$ changing the location of the sensors. This case will be referred to as DA-LES-1-BC. The size of the region and the sensor distribution strategy is the same previously employed, but the box is now placed upstream for $x \in [0.5,\ 6.5]$ in Λ units. So, the closest sensors to the inlet are two elements away from the boundary if we consider that the LES resolution in the streamwise direction is $\Delta x = \Lambda/4$.
4. **DA combining information from slightly different test cases**. One of the most appealing characteristics of Data Assimilation is the reconstruction of a state estimation from data obtained from different sources, which can be produced by different set-ups. While this aspect usually summons the idea of CFD-experiments integration, it remains valid for CFD-CFD estimation. For example, one could expect that boundary conditions studied for DNS cannot be systematically employed for LES. So, the sequential estimator will be tested integrating DNS data in a very simplified LES model, where in particular the velocity field at the inlet is reduced to a classical hyperbolic tangent profile in the streamwise direction. The capability of the sequential DA tool to generate a physical turbulent flow, even when the governing inlet information is missing, will be investigated. To this aim, a classical LES and two Kalman estimators based on the simplified LES model will be performed.

4 Results & Discussion

The results obtained via the Kalman estimator runs are compared with a classical LES and the DNS used to produce the samples. The analysis is focused on the velocity field features, both instantaneous and averaged. It is here reminded that the sequential Data Assimilation integrates the instantaneous velocity fields.

4.1 State estimation of the statistical properties of the flow

The attention is first focused on the prediction of the statistics of the velocity field U and in particular on its time-averaged behavior $\overline{U}$. The velocity profiles for $\overline{U_x}$, which have been averaged as well in the spanwise direction z, are shown against the normalized axis y/Λ. Results are shown for the three different streamwise stations $x = 5,\ 10,\ 18$ in Λ units and they are shown in Figs. 3, 4 and 5, respectively. The style of the plot has been chosen to improve the clarity of the representation. So, DNS data are represented via a blue line with diamonds markers, the classical LES using a red line with square markers. The Kalman estimator results have been grouped with respect to colors. Simulations for $f_T = 1,\ 2,\ 5,\ 10$ i.e. high frequency assimilation are represented in black, while results for $f_T = 20,\ 50,\ 100,\ 200$ (low density for observation in time) are shown in gray.

Profiles in Fig. 3 have been sampled upstream with respect to the Data Assimilation region, which is included in $x \in [6,\ 12]$. The analysis of the global velocity profile in

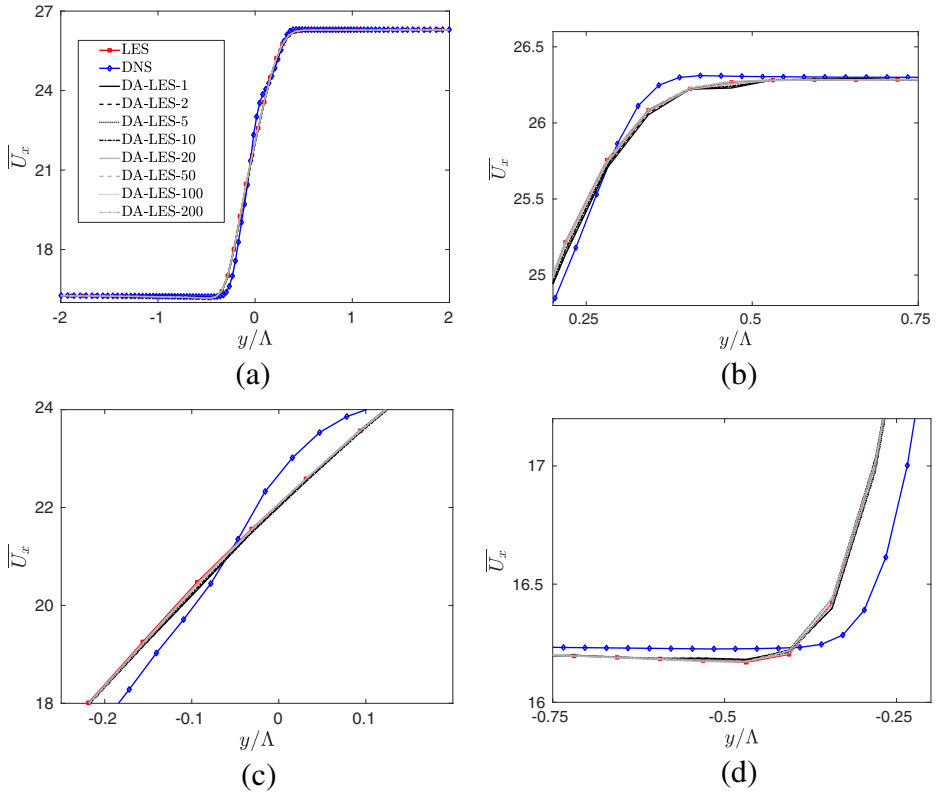

Fig. 3 Velocity profiles for the database of simulations, sampled for $x = 5\,\Lambda$. The streamwise velocity $\overline{U_x}$ is averaged in time and in the spanwise direction. **a** The complete velocity profile and zooms at **b** the top, **c** the center and **d** the bottom of the profile with respect to the normal direction y are shown, respectively

Fig. 3a and the three zooms in Fig. 3b–d show a marked difference in the behavior of the streamwise velocity. In general, the DNS prediction is clearly different from the rest of the simulations of the database, which mostly superpose. The minimal difference between classical LES and Kalman estimator is a signature of the governing effect of DA performed by the boundaries, which are much more intense than upstream transfer of information via Kalman filter. One could argue that the much higher number of elements of the boundary and their spatial compactness, as well as the fact that they are applied at each time step, provides a stronger effect on the flow when compared with the field effect produced by the estimator. Also, the complex velocity profile imposed at the inlet leads to the emergence of coherent structures (see Fig. 1a) which, because of their strong organization, are not easily disrupted by the assimilation process. Further analysis of the profiles reveals interesting features. First, the bump behavior observed for the DNS in Fig. 3c is not visible in any of the other simulations. The LES and the Kalman estimator provide a much more regular profile, which clearly exhibits turbulent features which should be observed significantly downstream. In addition, the return towards the unperturbed asymptotic conditions U_1 and U_2 is slower for the reduced-order simulations (see Fig. 3b and d), which implies a faster

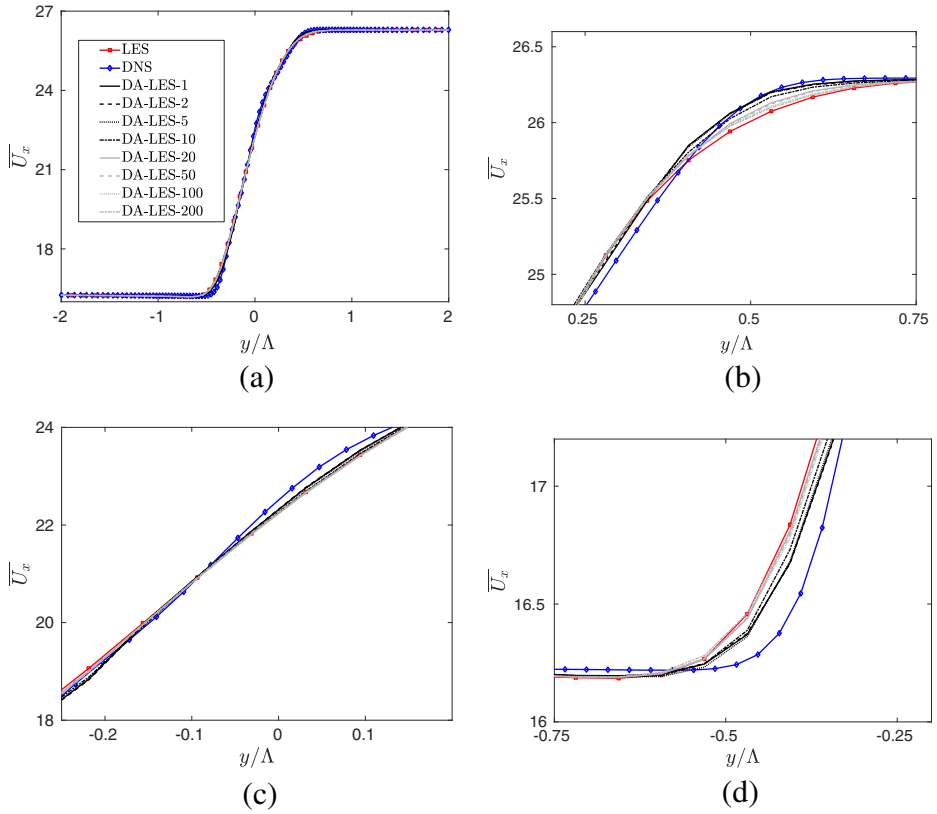

Fig. 4 Velocity profiles for the database of simulations, sampled for $x = 10\,\Lambda$. The streamwise velocity $\overline{U_x}$ is averaged in time and in the spanwise direction. **a** The complete velocity profile and zooms at **b** the top, **c** the center and **d** the bottom of the profile with respect to the normal direction y are shown, respectively

growth of the wake. These two features are associated with the unwanted effects of the sub-grid model viscosity ν_{SGS} which is triggered by the important velocity gradients imposed at the inlet.

The analysis of the results in Fig. 4 provides quite a different picture. In this case, data are sampled for $x = 10\,\Lambda$ in the middle of the observation region, where DNS observation is integrated. Generally speaking, the classical LES results are the most distant from the DNS prediction and the transition towards the two asymptotic states is slow i.e. the predicted wake is thicker. Data assimilated solution with high density in observation (black line) exhibit a relatively good agreement with DNS data, in particular for the upper surface of the wake shown in Fig. 4b. Extensive analysis of the results pointed out the effect in the prediction of the Kalman estimator is gradual improving downstream from $x = 6\,\Lambda$, where barely any effect is visible. In addition, it appears that the black lines almost exactly superpose, with only the simulation DA-LES-10 showing some difference. For this case, the period between successive assimilations is $\Delta T = 10 \cdot 10 \cdot \Delta t = t_A$. Thus, one could argue if the frequency of assimilation of $f_T = 2\,t_A^{-1}$ is a good estimation for a threshold of convergence of the estimator. $t_A = 2\Lambda/(U_1 + U_2)$ is the characteristic advection time and it represents the time in which a coherent structure is pushed downstream of a characteristic length Λ,

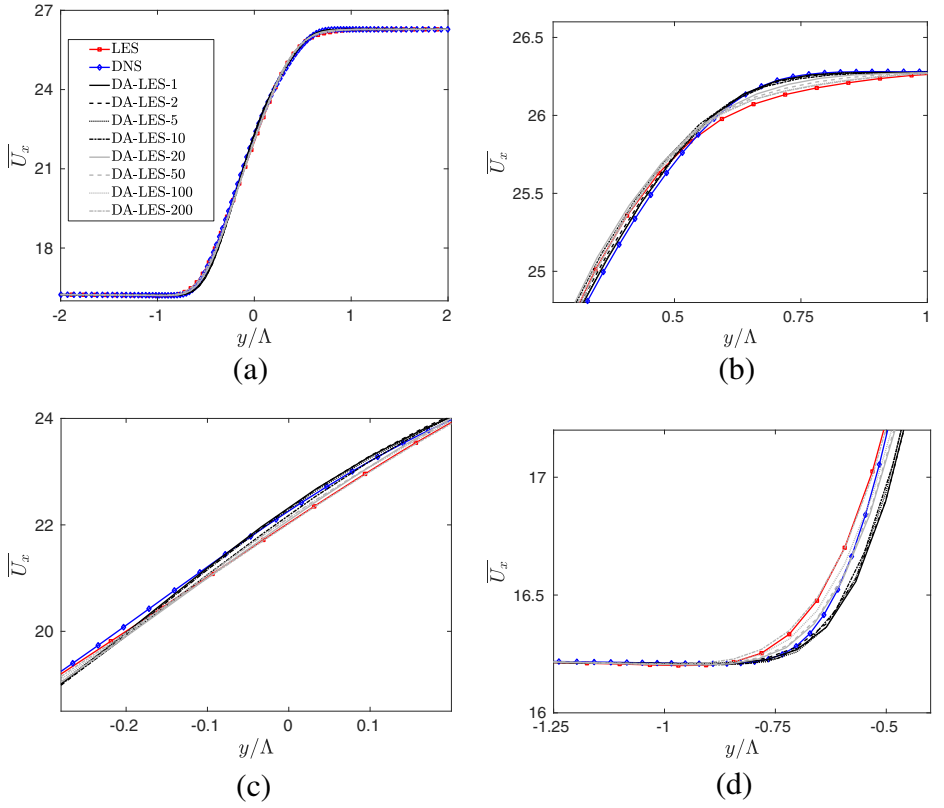

Fig. 5 Velocity profiles for the database of simulations, sampled for $x = 18\,\Lambda$. The streamwise velocity $\overline{U_x}$ is averaged in time and in the spanwise direction. **a** The complete velocity profile and zooms at **b** the top, **c** the center and **d** the bottom of the profile with respect to the normal direction y are shown, respectively

which is associated with primary Kelvin-Helmholtz instabilities. This threshold value can also be associated with the characteristic shear time $f_T \approx 8\,t_S^{-1}$, $t_S = 2\Lambda/(U_1 - U_2)$. For frequencies of acquisition lower than this threshold, the state estimation appears to converge towards the classical LES prediction, which can be deduced by the observation of the gray lines. However, preliminary tests showed how this evolution can exhibit non-linear features which are sensitive to the placement of the sensors, in particular for acquisition frequencies slightly larger than the threshold identified. Thus, one should perform sequential state estimation using acquisition frequency which at least match the physical evolution of the flow, whenever possible. Lower acquisition frequencies could result in a worst prediction when compared with classical reduced-order numerical simulation. This information is valuable, because it provides a first link between the numerical process of state estimation and the physical behavior of the flow.

Results for the streamwise section $x = 18\,\Lambda$ are shown in Fig. 5. Here, data are sampled well outside the assimilation region, but sufficiently upstream with respect to the outlet boundary condition. Here the trend is very similar to observations for Fig. 4, which shows how the Kalman estimator is more efficient in propagating the information in the advective direction or at least far from the inlet. However, if one has a look at Fig. 5d the high frequency estimators actually under-predict the thickness of the wake close to the

low momentum asymptotic flow. This counter intuitive result (one would expect the performance of the estimator to get closer to LES moving downstream from the sensors) will be further discussed in Section 4.2 with the analysis of the instantaneous flow fields.

At last, the statistical organization of coherent structures is investigated. To do so, the time averaged velocity $\overline{U_y}$ is plotted over $y-z$ planes for the three streamwise stations of investigation $x = 5,\ 10,\ 18\,\Lambda$. Results for $x = 5\,\Lambda$ are shown in Fig. 6. Consistently with previous observations for $\overline{U_x}$, none of the reduced order simulations really matches the DNS results before the observation region. In addition, one can see that classical LES and DA-LES-200 produce almost identical results i.e. the assimilation process is negligible. However, significant differences are observed for the streamwise station $x = 10\,\Lambda$. Here, results for the estimator DA-LES-1 in Fig. 7c are qualitatively similar to DNS in Fig. 7a and, despite the significantly lower resolution, the structural organization is clearly recognizable. On the other hand, classical LES and estimator DA-LES-200 fail to capture structural features of the flow. A quantitative measure of the error has been obtained calculating L2 norms:

$$\int_{x=10} \frac{||\overline{U_y}^{DA1} - \overline{U_y}^{DNS}||}{||\overline{U_y}^{DNS} + 10^{-16}||}\, dydz = 3.4 \times 10^{-3}$$

$$\int_{x=10} \frac{||\overline{U_y}^{LES} - \overline{U_y}^{DNS}||}{||\overline{U_y}^{DNS} + 10^{-16}||}\, dydz = 4.8 \times 10^{-3}$$

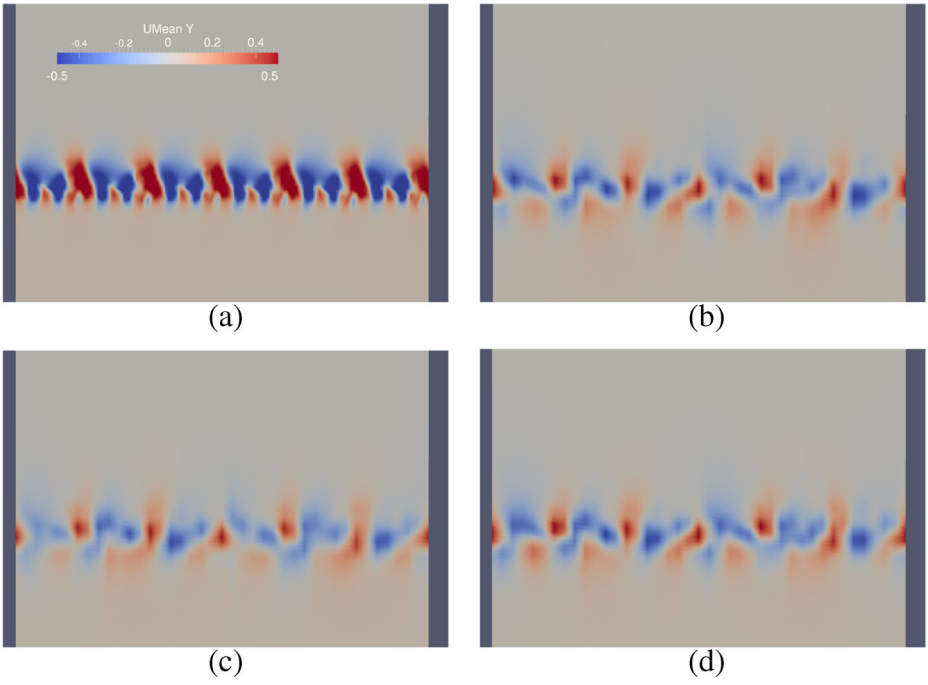

Fig. 6 Velocity profiles for the database of simulations, sampled for $x = 5\,\Lambda$. The normal velocity $\overline{U_y}$ is averaged in time. Results for **a** DNS, **b** classical LES, **c** DA-LES-1 estimator **d** DA-LES-200 estimator are shown, respectively

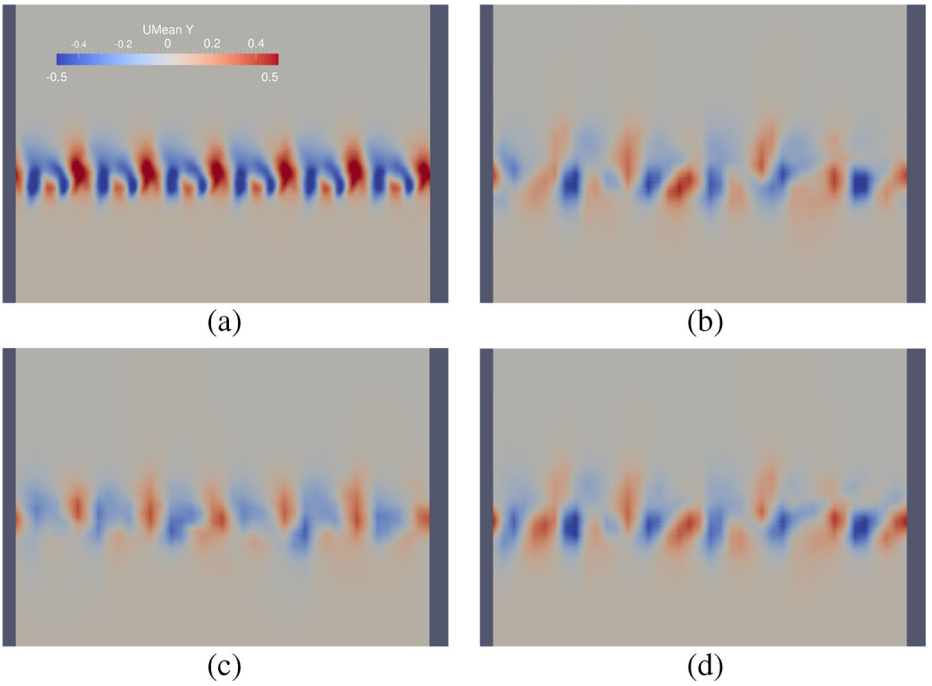

Fig. 7 Velocity profiles for the database of simulations, sampled for $x = 10\,\Lambda$. The normal velocity $\overline{U_y}$ is averaged in time. Results for **a** DNS, **b** classical LES, **c** DA-LES-1 estimator **d** DA-LES-200 estimator are shown, respectively

These results reinforce the idea that Data Assimilation is not just locally beneficial in space and time, but it is also efficient in capturing more global features of the flow. Results outside the assimilation region for $x = 18\,\Lambda$ are shown in Fig. 8. Again, the results for the estimator DA-LES-1 qualitatively match the DNS prediction, confirming that the Data Assimilation strategy is efficient in the whole physical domain, whenever it is not damped by other features of the simulation such as the boundary conditions. The quantification of the error via L2 norm provides the following result:

$$\int_{x=18} \frac{||\overline{U_y}^{DA1} - \overline{U_y}^{DNS}||}{||\overline{U_y}^{DNS} + 10^{-16}||}\, dydz = 7.4 \times 10^{-3}$$

$$\int_{x=18} \frac{||\overline{U_y}^{LES} - \overline{U_y}^{DNS}||}{||\overline{U_y}^{DNS} + 10^{-16}||}\, dydz = 1.61 \times 10^{-2}$$

4.2 Analysis of the instantaneous flow field

Discussion about the statistical properties of the flow field in Section 4.1 is now further extended in the light of the analysis of the physical properties of the instantaneous flow field. In particular, instantaneous isocontours of the velocity magnitude on a $x - y$ plane sampled for $z = 3\,\Lambda$ are reported in Fig. 9. One should keep in mind that, because of the spanwise inlet perturbations introduced, only qualitative elements of discussion should be deduced by

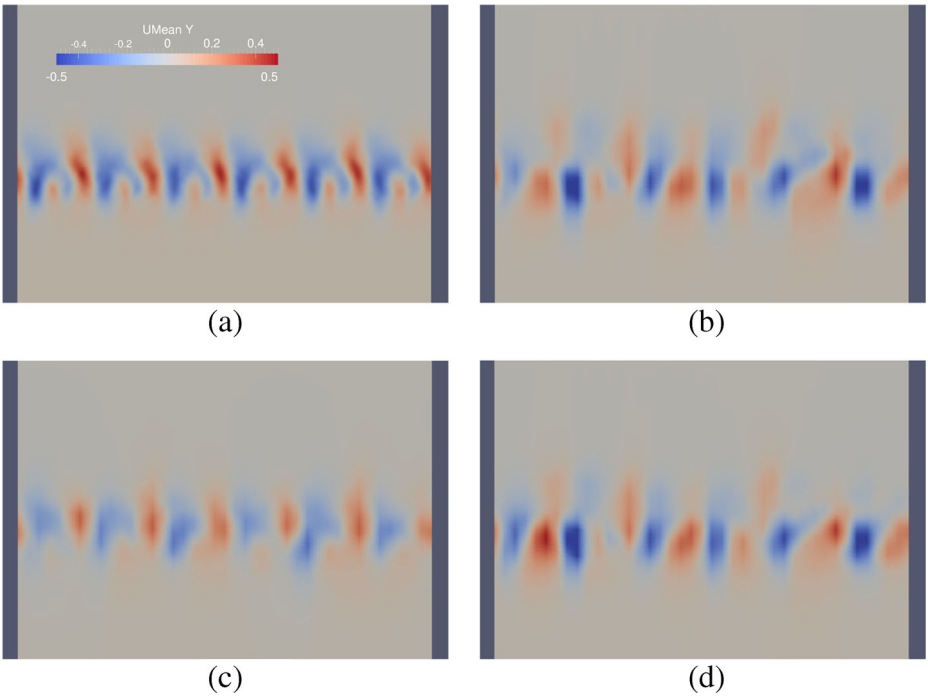

Fig. 8 Velocity profiles for the database of simulations, sampled for $x = 18\,\Lambda$. The normal velocity $\overline{U_y}$ is averaged in time. Results for **a** DNS, **b** classical LES, **c** DA-LES-1 estimator **d** DA-LES-200 estimator are shown, respectively

a 2D visualization of an instantaneous fully 3D field. Here, data for the final time step for $t = 200\,t_A$ are shown. The reference DNS contours are provided in Fig. 9a. The classical LES solution in Fig. 9b appears to be significantly different. In fact, much larger organized structures tend to emerge very close to the inlet boundary and they are responsible for the general larger width of the mixing region which was discussed in Section 4.1. Results for the estimator DA-LES-1 are now investigated (Fig. 9c). In the inlet region, a physical organization of the flow similar to the classical LES case is observed. However, proceeding inside the assimilation region, the flow clearly exhibits a strong structural modification, which is conserved moving downstream. This prediction is more similar to the DNS instantaneous isocontours, clearly at a reduced resolution. It is also important to observe that the physical configuration is continuous, and it is not possible to guess where the sensors are placed. This result is mainly due to the effective propagation of information by Kalman filter and Poisson equation. The under prediction of the wave thickness downstream which was previously observed may be related to the different structural organization produced by the estimator. This aspect will be further investigated with the isocontours of the sub-grid scale viscosity ν_{SGS}. Results for the estimator DA-LES-200 are shown in Fig. 9d. In this case, a strong resemblance to classical LES is observed, which justifies the almost identical statistical results obtained. In this case, the assimilation process is performed every 20 characteristic advection times. One could think that, in this case, the assimilation process

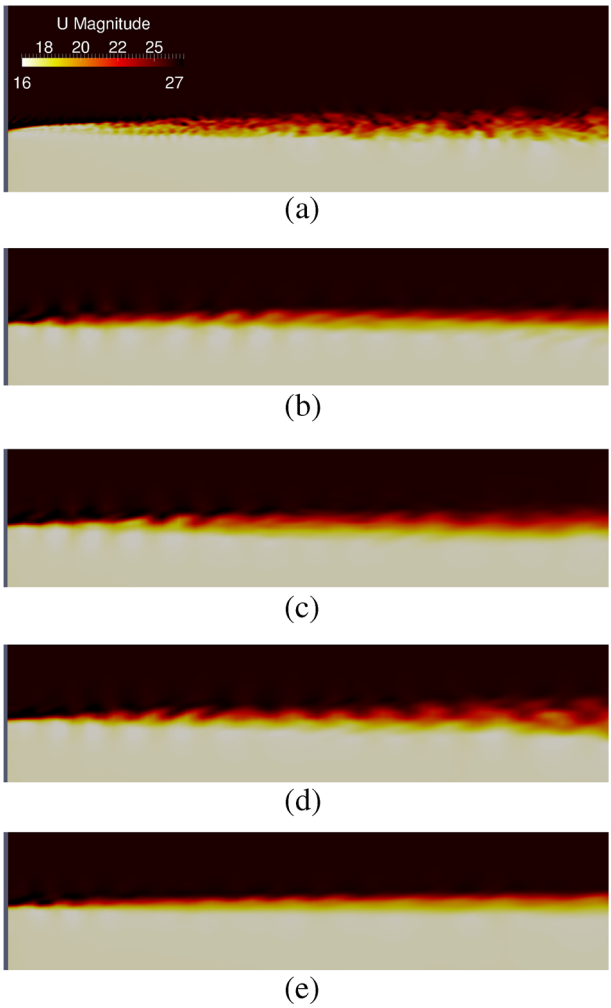

Fig. 9 Instantaneous velocity profiles for the database of simulations, sampled on an $x - y$ plane. Zooms are performed to improve the visualization and in particular $x \in [0,\ 18]\ \Lambda$. Results for **a** DNS, **b** classical LES, **c** DA-LES-1 estimator, **d** DA-LES-200 estimator and **e** DA-LES-1-BC estimator are shown, respectively

is nothing more than a spurious perturbation for the flow, which is transported downstream in the same way the initial conditions are at the beginning of the simulation. One common feature between the LES and the two estimators previously considered is the behavior in the inlet region. The inlet is dominant right until the beginning of the assimilation region. This result is due to the complex information prescribed, as well as because of the number of *sensors* which is much larger and dense in space for the boundary condition. So, the results for the estimator DA-LES-1-BC in Fig. 9e are now investigated. For this configuration data assimilation is performed every 10 time steps, but the cloud of sensors is included in $x \in [0.5,\ 6.5]$ i.e. much closer to the inlet. In this case no discontinuity or instability is observed, but one can see that the upstream organization of the flow does not exhibit the big

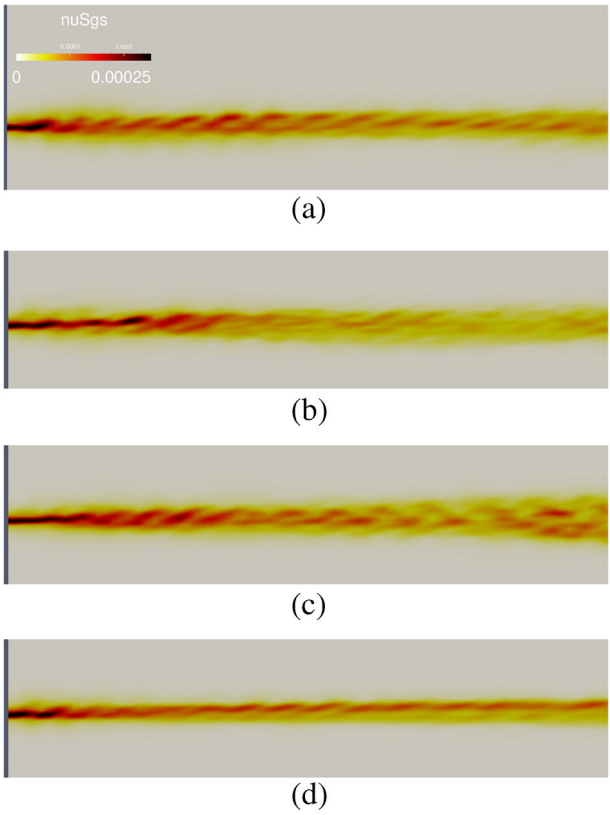

Fig. 10 Instantaneous ν_{SGS} profiles for the database of simulations, sampled on an $x - y$ plane. Zooms are performed to improve the visualization and in particular $x \in [0, 18]\ \Lambda$. Results for **a** classical LES, **b** DA-LES-1 estimator, **c** DA-LES-200 estimator and **d** DA-LES-1-BC estimator are shown, respectively

structures characterizing the other reduced-order simulations. The structures do not really form downstream either, which appears to result in an under-prediction of the thickness of the wake.

These physical observations are now further investigated via the analysis of the sub-grid scale viscosity ν_{SGS}, which is shown is Fig. 10. For the classical LES and the estimator DA-LES-200 (Fig. 10a and c) the maximum of ν_{SGS}, which is approximately 10ν, superposes with the coherent structures observed in the velocity field representation. For the high frequency estimators DA-LES-1 and DA-LES-1-BC in Fig. 10b and d this organization is absent and the velocity gradients are smoothed. The Smagorinsky model imposes a linear relation between the magnitude of the velocity gradients and the sub-grid scale viscosity. This aspect results in a slight under prediction of ν_{SGS} which has been derived by observation of several instantaneous solutions. Observation of Fig. 10 indicates that the under prediction of ν_{SGS} appears to be more intense close to the low momentum asymptotic flow. This behavior is arguably responsible for the under-prediction of the thickness close this region, where coherent structures dynamics are more important with respect to the pure advection of the flow and the sub-grid scale diffusion should be enhanced.

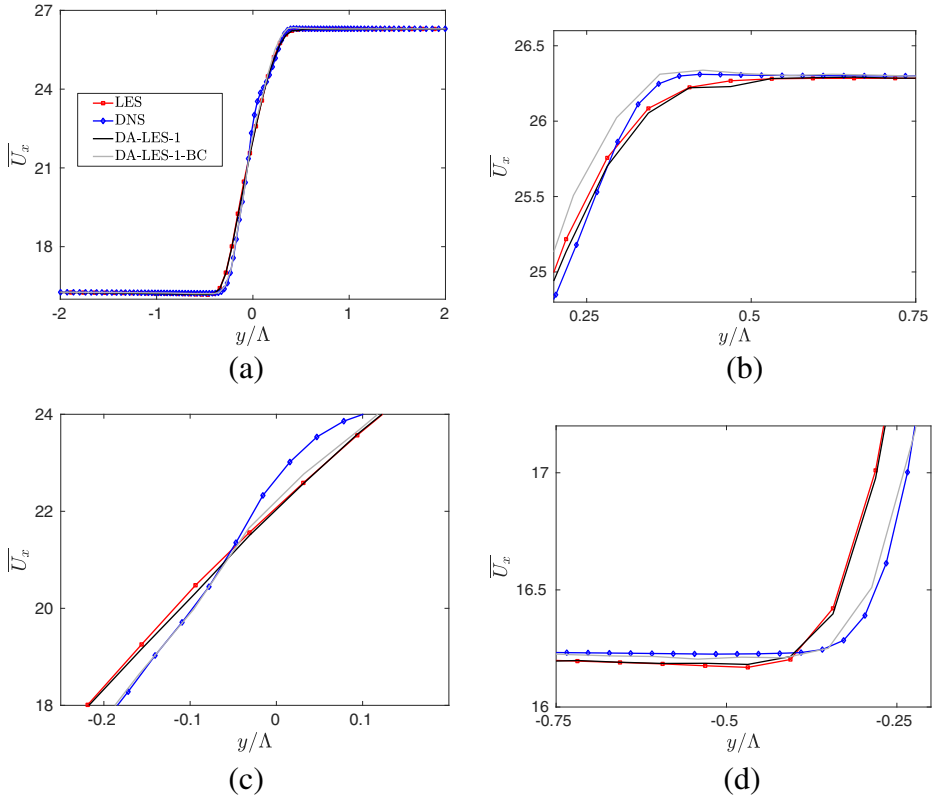

Fig. 11 Velocity profiles $\overline{U_x}$ sampled for $x = 5\ \Lambda$. The sensitivity to the position of sensors is investigated. **a** The complete velocity profile and **b–d** zooms are shown, respectively

The analysis is concluded by a second observation of the averaged velocity profiles. In this case, the analysis is limited to the simulations DNS, LES, DA-LES-1 and DA-LES-1-BC and for $x = 5,\ 10\ \Lambda$ (the conclusions for the last downstream section are similar to the case $x = 10\Lambda$). Results for $x = 5\Lambda$ are shown in Fig. 11. In this case, DNS data is here assimilated for the estimator DA-LES-1-BC. The results for the average velocity profiles are consistent with the discussion previously developed for the instantaneous flow fields, and the upstream sensor positioning is beneficial to improve the flow prediction. The under prediction of the upper limit of the wake observed for the estimator DA-LES-1-BC may be related with the representation of the bump, which is not very well captured probably because of resolution effects. Results for $x = 10\Lambda$ are now investigated in Fig. 12. As expected, the estimator DA-LES-1-BC exhibits under prediction of the thickness of the wave because of the poor interaction between the state estimation and the sub-grid scale model. However, the prediction of the estimator DA-LES-1-BC appears to be more precise when compared with the classical LES, even if DNS data is not integrated in this streamwise section. In summary, the analysis of Figs. 11 and 12 suggests that strategies for sensor positioning should target upstream locations with respect to turbulence transition, when state estimation is obtained via reduced-order modeling. This is particularly true if optimization / tuning of the model coefficients can be performed.

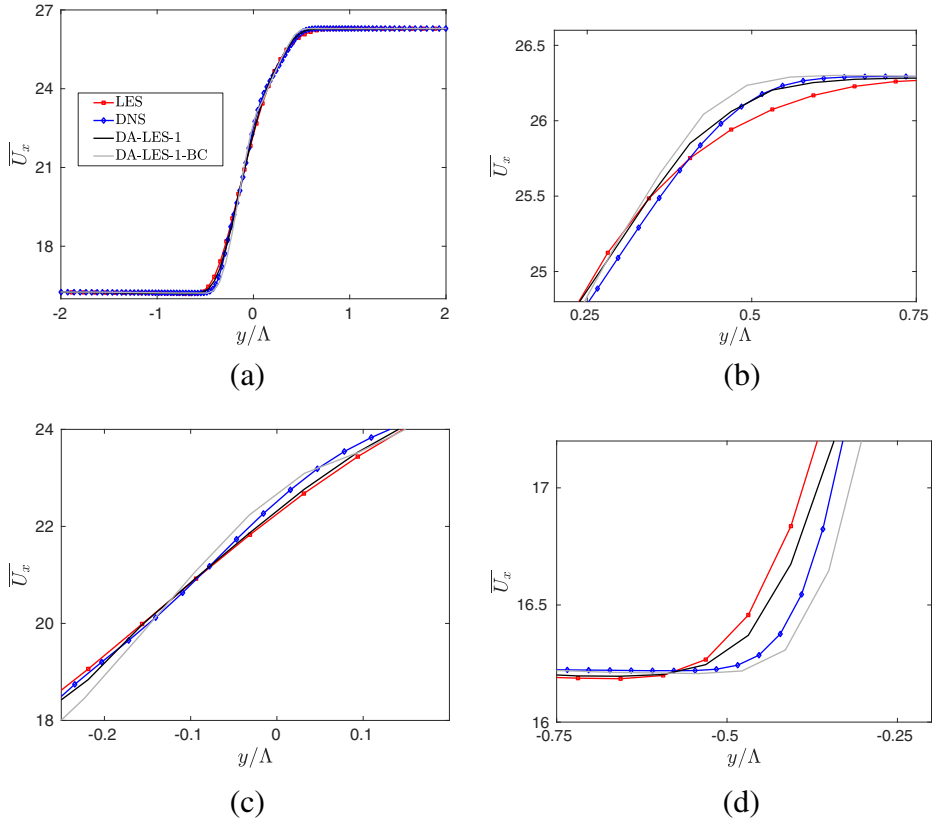

Fig. 12 Velocity profiles $\overline{U_x}$ sampled for $x = 10\,\Lambda$. The sensitivity to the position of sensors is investigated. **a** The complete velocity profile and **b**–**d** zooms are shown, respectively

5 Data Assimilation Combining Information from Slightly Different Test Cases

In this section the numerical test case for LES and DA estimator is slightly modified, in order provide a more realistic example of sequential state estimation using different sources of information. The changes to the set-up are:

1. The size of the grid and the mesh resolution is unchanged, but the physical domain is now included in $[x \times y \times z] \in [0.8, 24.8 \times -9, 6 \times -3, 3]$ in Λ units. This implies that the physical domain has been shifted of $4/5$ length units in the streamwise direction, so that the mesh elements are not aligned anymore.
2. The inlet condition is dramatically simplified, just keeping the classical hyperbolic tangent profile for the velocity U_x. So, U_x is a function of y only. The other velocity components U_y and U_z are set to zero.
3. The flow in the physical domain is initialized using the same velocity profile imposed at the inlet.

A reference LES simulation (LES-D-4T) is run using a time step $\Delta t' = 4\Delta t$, so that the resulting $CFL \approx 0.3$ is closer to the value observed for DNS. In addition, two DA

estimators are run, namely DA-LES-2-D and DA-LES-2-D-4T. Both estimators integrate DNS data with a constant assimilation period of $20\Delta t$ using the cloud of sensors initially employed in the range $x \in [6,\ 12]$. The only difference between the two estimators is that for DA-LES-2-D the time step is equal to Δt (and so observation is assimilated every 20 time steps) while DA-LES-2-D-4T performs a time advancement with a time step equal to $\Delta t'$, assimilating each 5 time steps.

Qualitative results at the end of the simulations for $t = 200\, t_A$ are shown in Fig. 13 for the isocontours of the Q criterion. A first important observation is that the classical LES results reported in Fig. 13b do not match the structural organization of the flow obtained with DNS. One can barely see the emergence of three dimensional effects. This result is clearly produced by the lack of information that is provided at the inlet for this case. On the other hand, both the estimators provide a representation which is consistent with the DNS visualization. Core differences between Fig. 13c and d cannot be highlighted via this qualitative representation. In addition, one can see that the structural coherent organization of the flow is propagated well upstream the sensor region. One possible reason for this observation is that the simpler inlet boundary condition prescribed is not able to extend its governing effect far from the very proximity of the boundary. Thus, one can deduce that the interaction between boundaries and sequential state estimation is affected (if not governed) by

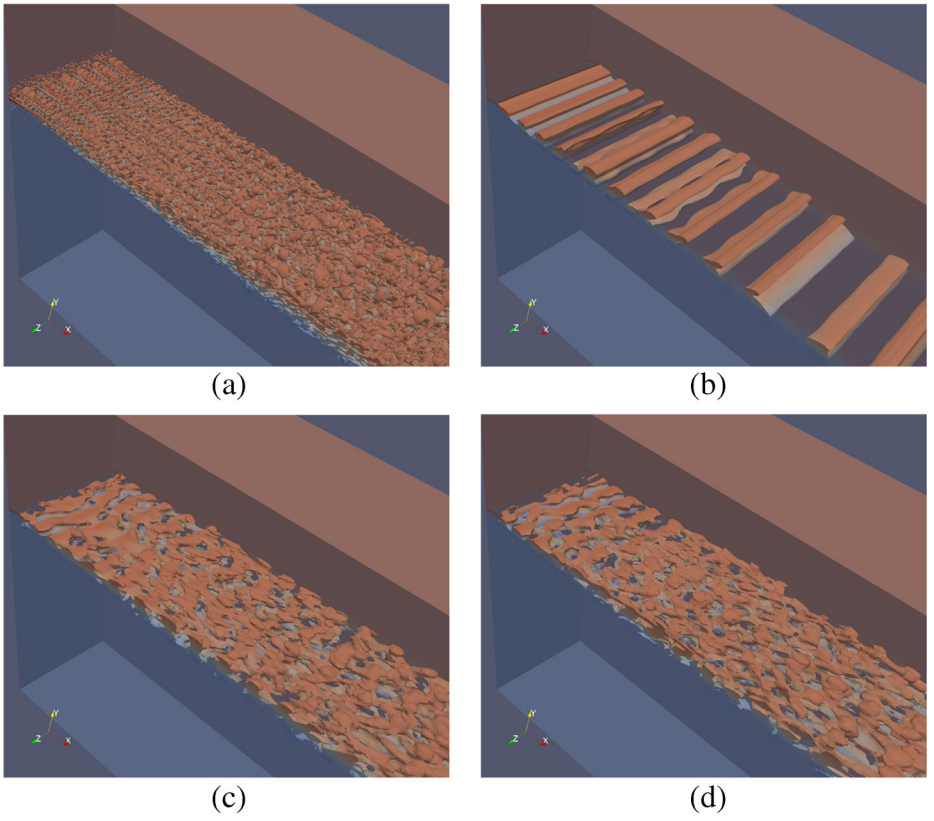

Fig. 13 Instantaneous isocontours of the Q criterion for $t = 200t_A$. Results for **a** DNS, **b** classical LES (LES-D-4T), **c** estimator DA-LES-2-D and **d** estimator DA-LES-2-D-4T are shown, respectively. The DNS velocity profile is shown in transparency in each visualization

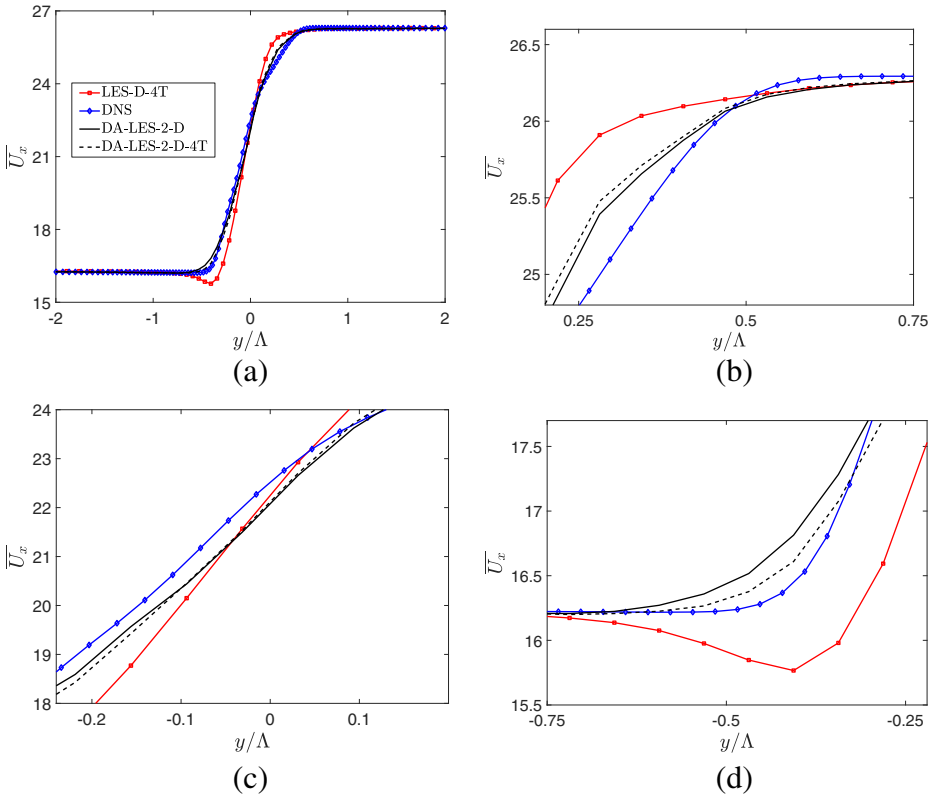

Fig. 14 Velocity profiles $\overline{U_x}$ sampled for $x = 10\,\Lambda$. High precision DNS data are assimilated in a slightly different numerical test case. **a** The complete velocity profile and **b**–**d** zooms are shown, respectively

the physical features that are prescribed. Data integration in the physical domain combined with classical boundary conditions used in CFD could provide the same level of accuracy in flow physical representation of advanced realistic boundaries, which is one of the open challenging aspects in the future of HPC for industrial applications.

At last, the averaged streamwise velocity profiles are shown in Fig. 14 for $x = 10\,\Lambda$. These results confirm the lack of accuracy of the results for LES-D-4T, which does not predict the progressive transition of the flow towards turbulence. The comparison of the estimators highlights some differences, which most probably raise from the different values of the time step affecting the determination of the model uncertainty matrix Q (see Eq. 13).

6 Conclusions & Perspectives

In the present work, the sensitivity of the performance of a reduced order Kalman filter estimator to the time density of available observation has been studied. Its capabilities have been validated with the analysis of the turbulent spatially evolving mixing layer test case. The observer produces a smooth, physical flow condition via integration of different sources of information. Even if the observation region is limited in space (only 1000 sensors out of 340 000 mesh elements), the propagation of information via Poisson equation is efficient and

the flow prediction is definitely more accurate. In addition, the increase in computational resources with respect to the model is very limited (of the order of 15%).

The main result deduced by the present analysis is that if the time between successive data integration is sufficiently small with respect to the characteristic advection time, the estimator produces a converged augmented configuration. However, it appears that once a threshold value is passed (approximately a period of $0.5t_A$ in this case) the performance of the estimator may not smoothly return towards the pure model performance (in this case the classical LES). This aspect is connected with the interaction between the estimated flow field and the sub-grid scale model, which can lead to counter-intuitive results. In the case of this analysis, the velocity gradients obtained via state estimation close to the lower momentum asymptotic flow are not sufficient to produce a sufficiently large sub-grid scale viscosity ν_{SGS}, which results in an under-prediction of the size of the wake. This is exactly the opposite behavior of the classical LES, which exhibits a systematic over prediction of the wave thickness. These observations stress how, while the state estimation via Kalman filtering is globally beneficial, further improvement could be achieved integrating some optimization techniques to tune the free parameters of the simulation, such as coefficients in the boundary conditions or in the sub-grid scale model.

In addition, the interaction between boundary conditions and the Kalman filter has been investigated. While no numerical instability has been observed, the inlet boundary may prove to be dominant upstream of the sensor region. A possible explanation is that the boundary is composed by a larger number of elements, compact in space which may impose a complex information at each time step. The application of sensors close to the boundary (or at least upstream with respect to transition to turbulence) has proven to be a first strategy of improvement for sequential state estimation. On the other hand, the simplification of the inlet boundary condition allowed to propagate further upstream the state estimation. Thus, the quality of the information provided at the inlet influences the interaction between the estimator and the boundary itself and so the state estimation. This aspect suggests that aiming for realistic and complex boundary conditions may not be the best strategy to obtain high-fidelity results, if sequential integration of data in the physical domain can be performed.

Compliance with Ethical Standards The research work has been developed employing computational resources within the framework of the project gen7590-A0012A07590 DARI-GENCI.

Conflict of Interest The author declares that he has no conflict of interest.

Appendix A: Reduced Order Kalman Estimator

The essential features of the reduced order model based on Kalman filtering are here described. The estimator exploits structural similarities between the discrete Kalman filter [19] schemes and numerical algorithms for the resolution of incompressible turbulent flows.

The Kalman Filter is a sequential estimator which provides an optimal state estimation $\hat{\mathbf{U}}$ of a random process $\mathbf{U}$ when a physical *model* and available *observation* $\mathbf{Z}$ are provided. Considering time advancement from the instant $n-1$ to n, we have:

$$\mathbf{U}_n = \Psi_n \mathbf{U}_{n-1} + B_n \mathbf{c}_n + \mathbf{W}_n \tag{1}$$

$$\mathbf{Z}_n = H_n \mathbf{U}_n + \mathbf{V}_n \tag{2}$$

Equation 1 is referred to as *model* and Eq. 2 as *observation*. The term $B_n\,\mathbf{c}_n$ in Eq. 1 represents the effect of a *controller* over the prediction of the random process via model. The terms $\mathbf{W}_n = \mathcal{N}(0,\, Q_n)$ and $\mathbf{V}_n = \mathcal{N}(0,\, R_n)$ represent zero-mean uncertainties which affect the model and the observation, respectively. They are quantified via the covariance matrices Q and R. The higher the covariance, the lower the confidence in the associated information. While the matrices could potentially exhibit any structure, they are usually assumed to be diagonal in fluid mechanics applications [1, 10]. In addition, a state estimation error covariance matrix $P = E((\mathbf{U} - \hat{\mathbf{U}}) \times (\mathbf{U} - \hat{\mathbf{U}})^T)$ provides a measure of the confidence in the state estimation. The sequential estimator performs a time advancement through two steps:

1. A *prediction* step, where the model is used to advance in time the physical state. Observation for the time step n is not included yet:

$$\hat{\mathbf{U}}_{n|n-1} = \Psi_n \hat{\mathbf{U}}_{n-1} + B_n\,\mathbf{c}_n \tag{3}$$

$$P_{n|n-1} = \Psi_n\, P_{n-1|n-1}\, \Psi_n^T + Q_n \tag{4}$$

2. An *update* step, where available observation is integrated in the model prediction to obtain the *augmented* state:

$$\hat{\mathbf{U}}_{n|n} = \hat{\mathbf{U}}_{n|n-1} + K_n \left(\mathbf{Z}_n - H_n\, \hat{\mathbf{U}}_{n|n-1}\right) \tag{5}$$

$$P_{n|n} = (I - K_n\, H_n)\; P_{n|n-1} \tag{6}$$

The central element controlling the prediction is the Kalman gain K_n. Mathematical manipulation shows that, if $\mathbf{W}_n$ and $\mathbf{V}_n$ are random Gaussian variables, the minimization of P can be obtained using the optimal gain

$$K_n = P_{n|n-1}\, H^T\, S_n^{-1}\,, \qquad S_n = H_n\, P_{n|n-1}\, H_n^T + R_n \tag{7}$$

So, the Kalman gain K performs a weighted combination of model prediction and observation, accounting for the level of confidence in the different sources. While this strategy is extremely efficient, Eq. 7 shows that matrices inversions must be performed in order to calculate P. Considering the degrees of freedom needed to perform numerical simulations of turbulent flows, a full resolution for P is prohibitive. CFD solvers are usually optimized for the resolution of Navier–Stokes equations over meshes of million of elements. In addition, algorithmic strategies are usually employed in order to reduce the computational resources required. One popular scheme for the analysis of incompressible flows is the PISO algorithm [20, 21], which is based on implicit time discretization plus a local linearization in time of the non-linear term. This scheme is based on a two step resolution:

1. A *predictor* step, where the momentum equation is resolved to obtain a first estimation of the velocity field $\mathbf{U}$:

$$\mathbf{U} = \frac{\Phi(\mathbf{U})}{a_P} - \frac{\nabla p}{a_P} \tag{8}$$

   where p is the normalized pressure and Φ indicates the resulting matrix form of the numerical discretization, which includes the source velocity information from the previous time step. a_P is a numerical coefficient resulting from the finite volume discretization of the derivative of the velocity fields and it includes at least a time-discretization component and a spatial diffusion component.
2. A *corrector* step, where a Poisson pressure equation is solved:

$$\nabla \cdot \left(\frac{\nabla p}{a_P}\right)_f = \sum_f S \times \left(\frac{\Phi(\mathbf{U})}{a_P}\right)_f \tag{9}$$

the subscript f indicates a calculation on the center of the face of the mesh element. A resolution loop for equations 8 - 9 is iteratively performed until convergence for the pressure gradient term is achieved and the velocity field complies with both the momentum equation and the zero-divergence condition.

One striking observation is that, in this case, Eq. 8 is a true *model* equation for the velocity field of the flow and Eq. 9 acts as a controller equation for ∇p (which is connected with the term $B_n\,\mathbf{c}_n$ of Eq. 3) which ensures a zero-divergence condition for $\mathbf{U}$. In addition, the *predictor-corrector* resolution of the PISO scheme is reminiscent of the *prediction-update* structure of the Kalman filter. The similarity between the two algorithms has been exploited in order provide a joint formulation [10]:

1. First step, the momentum Eq. 8 and the time advancement for P in Eq. 4 are performed. This is equivalent to the *prediction* step of the Kalman filter. One must keep in mind that this operation, and in particular the time advancement of the matrix P, is performed for each time step of the model. This implies that the matrix P is constantly updated between successive assimilation procedures, accounting for the evolution of the matrix Ψ_n.
2. Second step, an iterative procedure is employed to determine the state estimation $\hat{\mathbf{U}}$. If observation is available for the present time step, this is equivalent to Eq. 5 of the *update* step of the Kalman filter. Defining $F = K\ (\mathbf{z} - H\,\mathbf{U})$ one obtains:

$$\hat{\mathbf{U}} = \mathbf{U} + K\ (\mathbf{z} - H\,\mathbf{U}) = \frac{\Phi(\mathbf{U})}{a_P} - \frac{\nabla p}{a_P} + F \tag{10}$$

$$\nabla \cdot \left(\frac{\nabla p}{a_P}\right)_f = \sum_f S \times \left(\frac{\Phi(\mathbf{U})}{a_P} + F\right)_f \tag{11}$$

$$\mathbf{U} = \frac{\Phi(\mathbf{U})}{a_P} - \frac{\nabla p}{a_P} \tag{12}$$

   If observation is not available at the present time step, the loop is performed in any case, but $F = 0$ (i.e. a classical PISO algorithm is obtained).
3. Third step, the update of the error covariance matrix P is performed as in Eq. 6. Conversely to the first two steps, this last operation is performed only if observation has been integrated.

The most notable property of this algorithm is that the resulting *augmented prediction* naturally exhibits a zero-divergence condition for the velocity field. In addition, the pure PISO model prediction is obtained in case of absence of observation ($F = 0$). A simple optimization procedure is performed using $\hat{\mathbf{U}}$ as the source velocity field for the time step following the Data Assimilation.

This method exploits a linear strategy for state estimation which relies on the state matrix Ψ_n produced by the PISO algorithm. However, a similar local time linearization strategy is used in the *extended Kalman filter* [22], which is a non-linear version of the Kalman filter. The only difference is that while in the extended Kalman filter the non-linear model must be explicitly linearized when observation is available, this operation is already performed via the PISO algorithm in the present estimator.

As previously discussed, the implementation of the full strategy is computationally prohibitive because of the manipulation of the matrix P. However, the following strategies are employed to obtain a significant reduction in the computational resources demanded:

– The local linearization in time of the PISO algorithm naturally decouples the model prediction of the three velocity components, which are connected only via Poisson equation. As a result, if we consider a mesh of N elements, three matrices of size $N \times N$ instead of a matrix $3N \times 3N$ can be employed to describe Q, R and in particular P.
– If the model is a CFD tool, the matrix Q_n is assumed to be diagonal. This is a reasonable approximation if one considers the discretization / modeling error to be the main source of uncertainty in the CFD solver. Meldi and Poux [10] provided an empirical formula which allows to account for the local level of confidence in numerical simulation:

$$Q_n = C\left(1 + \frac{\nu_{SGS}}{\nu}\right)\Delta t^{ot}\,\Delta l^{os} \tag{13}$$

where C is a constant related with the discretization error, ν is the molecular viscosity of the flow and ν_{SGS} is the subgrid viscosity. Δt and Δl represent characteristics measures of the discretization step in time and space, respectively, and ot and os represent the order of precision of the discretization procedure. The matrix R_n is usually assumed to be diagonal as well, unless some information about the correlation of uncertainties in different sensors is provided.
– The state matrix of the model Ψ, which can be obtained via manipulation of the operator Φ in Eq. 8, is diagonally dominant. This means that diagonal elements are close to the unity in value and off diagonal elements are very small. In these conditions, it is possible to observe that the values of P corresponding to the zeros of the matrix $\Psi + \Psi^T$ are negligible too. So, one possible strategy is to conserve the correlation of a variable only to the variables playing a role in its state advancement, which means the neighbor mesh elements. In particular, Meldi and Poux [10] have shown how an efficient reduced order Kalman filter can be obtained working with a larger number of small size matrices, which are the size of the computational stencil of the mesh elements. This operation dramatically reduces the computational resources required.

While this filter is sub-optimal, the lack of performance is mitigated by the Poisson equation, which naturally diffuses the information in the physical domain. This strategy results in a very cost-efficient model, which is able to effectively integrate external observation in CFD runs.

References

1. Brunton, S.L., Noack, B.R.: Closed-loop turbulence control: progress and challenges. Appl. Mech. Rev. **67**, 050801 (2015)
2. Lumley, J.: Stochastic Tools in Turbulence. Academic Press, New York (1970)
3. Pope, S.: Turbulent Flows. Cambridge University Press, Cambridge (2000)
4. Sagaut, P.: Large-eddy Simulation for Incompressible Flows. An Introduction, 3rd edn. Springer, Berlin (2005)
5. Simon, D.: Optimal State Estimation: Kalman, H Infinity, and Nonlinear Approaches. Wiley, New York (2006)
6. Daley, S.B.: Atmospheric Data Analysis. Cambridge University Press, Cambridge (1991)
7. Foures, D.P.G., Dovetta, N., Sipp, D., Schmid, P.J.: A data-assimilation method for Reynolds-averaged NavierStokes-driven mean flow reconstruction. J. Fluid Mech. **759**, 404–431 (2014)
8. Mons, V., Chassaing, J.C., Gomez, T., Sagaut, P.: Reconstruction of unsteady viscous flows using data assimilation schemes. J. Comput. Phys. **316**, 255–280 (2016)

9. Suzuki, T., Yamamoto, F.: Hierarchy of hybrid unsteady-flow simulations integrating time-resolved PTV with DNS and their data-assimilation capabilities. Fluid Dyn. Res. **47**, 051407 (2015)
10. Meldi, M., Poux, A.: A reduced order Kalman Filter model for sequential Data Assimilation of turbulent flows. J. Comput. Phys. **347**, 207–234 (2017)
11. Colonius, T., Lele, S.K.: Sound generation in a mixing layer. J. Fluid Mech. **330**, 375–409 (1997)
12. McMullan, W.A., Gao, S., Coats, C.M.: A comparative study of inflow conditions for two- and three-dimensional spatially developing mixing layers using large eddy simulation. Int. J. Numer. Methods Fluids **585**, 589–610 (2007)
13. McMullan, W.A., Gao, S., Coats, C.M.: The effect of inflow conditions on the transition to turbulence in large eddy simulations of spatially developing mixing layers. Int. J. Heat Fluid Flow **30**, 1054–1066 (2009)
14. Meldi, M., Salvetti, M.V., Sagaut, P.: Quantification of errors in large-eddy simulations of a spatially evolving mixing layer using polynomial chaos. Phys. Fluids **24**, 035101 (2012)
15. Wang, Y., Tanahashi, M., Miyauchi, T.: Coherent fine scale eddies in turbulence transition of spatially-developing mixing layer. Int. J. Heat Fluid Flow **28**, 1280–1290 (2007)
16. Smagorinsky, J.: General circulation experiments with the primitive equations, I: the basic experiment. Mon. Weather Rev. **91**(3), 99–165 (1963)
17. Lilly, D.K.: The representation of small-scale turbulence in numerical simulation experiments. In: Proceedings of the IBM Scientific Computing Symposium on Environmental Sciences. 195–210 (1967)
18. Meldi, M., Lucor, D., Sagaut, P.: Is the Smagorinsky coefficient sensitive to uncertainty in the form of the energy spectrum? Phys. Fluids **23**, 125109 (2011)
19. Kalman, R.E.: A new approach to linear filtering and prediction problems. J. Basic Eng. **82**, 35–45 (1960)
20. Ferziger, J.H., Peric, M.: Computational Methods for Fluid Dynamics. Springer, Berlin (2002)
21. Issa, R.I.: Solution of the implicitly discretized fluid flow equations by operator-splitting. J. Comput. Phys. **62**, 40–65 (1986)
22. Julier, S.J., Uhlmann, J.K.: A new extension of the Kalman filter to nonlinear systems. In: Proceedings of AeroSense: The 11th International Symposium on Aerospace/Defence Sensing, Simulation and Controls (1997)